Negative-Sequence Current Capability in Low-Capacitance Cascaded H-Bridge Static Compensators With Optimal Third-Harmonic Circulating Current Injection

Ezequiel Rodriguez Ramos, *Member, IEEE*, Ramon Leyva, *Senior Member, IEEE*, Glen G. Farivar, *Senior Member, IEEE*, Christopher D. Townsend, *Member, IEEE*, and Josep Pou, *Fellow, IEEE*

***Abstract*—The cascaded H-bridge (CHB) low-capacitance static compensator (LC-StatCom) has a limited negative-sequence current injection capability compared to a conventional CHB StatCom, due to the comparatively larger oscillations on the capacitor voltages. Placing limits on the ability to provide negative-sequence current to the grid for a given capacitor size is required to prevent overmodulation. This article shows that these limits can be maximized by injecting an optimal third-harmonic circulating current. The effects of injecting the third-harmonic current on the capacitor voltages, both in balanced and unbalanced grid voltage conditions, are analyzed. Specifically, the procedure allows the knowledge of the potential capability of the LC-StatCom when injecting negative-sequence currents. The procedure is based on a linear programming approach. Although the procedure is applicable to any CHB StatCom, regardless of the submodule capacitor size, it is particularly important in LC-StatComs. To corroborate the proposed analysis, simulation and experimental results under balanced and unbalanced grid voltage conditions are presented.**

***Index Terms*—Cascaded H-bridge (CHB), circulating current injection, compensation region of negative-sequence currents, linear programming, multilevel converter, optimization methods, static compensator (STATCOM), thin dc capacitor.**

I. Introduction

THE low-capacitance static compensator (LC-StatCom) based on the cascaded H-bridge (CHB) converter has been previously proposed as an alternative to the conventional CHB StatCom, with the aim of reducing the capacitor size and improving efficiency [1], [2], [3], [4], [5], [6]. In the LC-StatCom, the H-bridge capacitance values are chosen to bound twice-fundamental-frequency oscillations in the capacitor voltages up to 40%–80% of the nominal dc voltage, whereas in a conventional CHB StatCom this bound is much lower (around 10%).

StatComs are required to operate both in balanced and unbalanced grid conditions [7], thus knowing the operating limits in both conditions, depending on the submodule capacitor size, is important. In addition to the capacitance and grid condition, the presence of the third-harmonic zero-sequence current (THZSC) also influences the operating limits. Furthermore, operating during unbalanced grid conditions requires the injection of a fundamental-frequency zero-sequence current (FFZSC) to maintain capacitor voltage control among the phase-arms of the CHB with delta connection [8], [9], [10], [11], [12], [13], [14]. Therefore, the study of the operating limits has to take into account the required FFZSC and the THZSC. The limits on the ability of LC-StatComs to provide negative-sequence current to the grid when no THZSC is injected have been studied in [14]. Specifically, Rodriguez Ramos et al.[14] showed cases in which an LC-StatCom delivering negative-sequence current overmodulates, while such cases would not overmodulate a conventional CHB StatCom with a larger capacitor size, or an LC-StatCom with an appropriate THZSC injection. Rodriguez Ramos et al. [14] employed an analytical procedure that takes advantage of the fact that there is always a perfect phase-alignment between the minimum capacitor voltage and the peak of the absolute value of the ac-side (grid) voltage in the phase-arm that would overmodulate. However, when THZSC is considered, this analytical procedure cannot be adapted as the mentioned phase-alignment is no longer guaranteed.

The operating points are limited when overmodulation appears. Fig. 1 shows voltage and current waveforms in the delta-connected LC-StatCom and in a conventional CHB StatCom providing unbalanced currents when the circulating current is only an FFZSC (without THZSC), as in [14]. Specifically, the absolute value of the ac-side voltages, in red, and the dc-side

Manuscript received 22 November 2022; accepted 23 December 2022. Date of publication 30 December 2022; date of current version 14 February 2023. This work was supported by the Office of Naval Research U.S. under DUNS Code: 595886219. Recommended for publication by Associate Editor K. Ma. *(Corresponding author: Ezequiel Rodriguez Ramos.)*

Ezequiel Rodriguez Ramos and Glen G. Farivar are with the Energy Research Institute, Nanyang Technological University, Singapore 639798 (e-mail: ezequiel001@e.ntu.edu.sg; gh_farivar@hotmail.com).

Ramon Leyva is with the Department of Electronic, Electrical and Automatic Engineering, Universitat Rovira i Virgili, 43007 Tarragona, Spain (e-mail: ramon.leyva@urv.cat).

Christopher D. Townsend is with the Department of Electrical, Electronic and Computer Engineering, University of Western Australia, Crawley, WA 6009, Australia (e-mail: chris.townsend@uwa.edu.au).

Josep Pou is with the School of Electrical and Electronic Engineering, Nanyang Technological University, Singapore 639798 (e-mail: josep.pou@ieee.org).

Color versions of one or more figures in this article are available at https://doi.org/10.1109/TPEL.2022.3233033.

Digital Object Identifier 10.1109/TPEL.2022.3233033

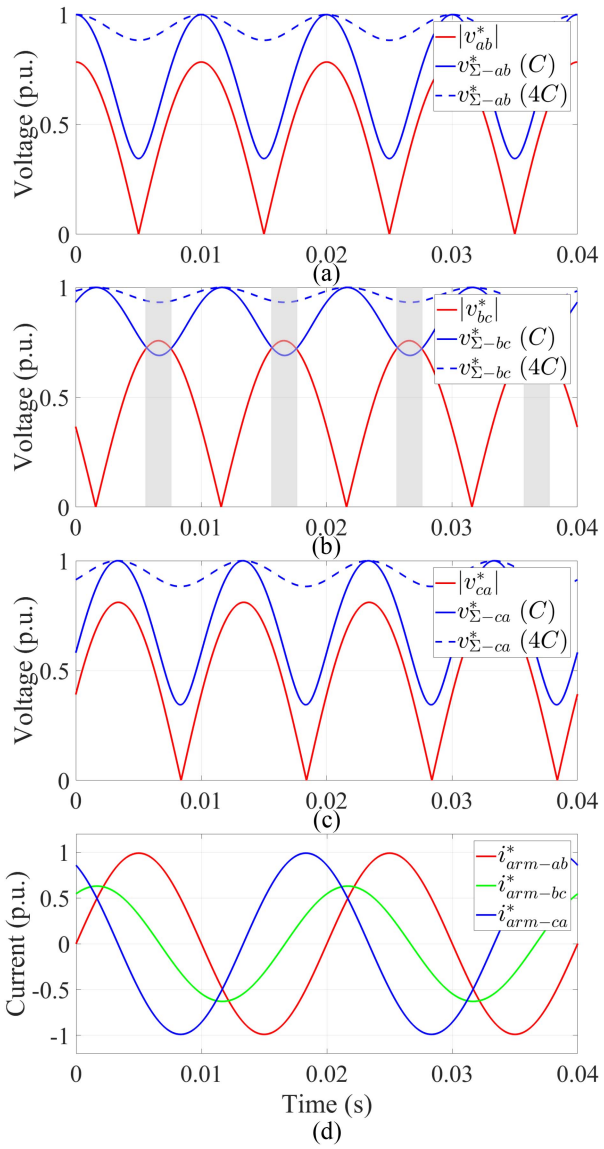

Fig. 1. Voltage waveforms on the ac-side v^*_x and on the dc-side $v^*_{\Sigma-x}$, for a delta-connected StatCom with capacitor size $4C$ (in dashed blue) and in an LC-StatCom with capacitor size C (in solid blue) in unbalanced conditions. (a) For phase-arm ab. (b) For phase-arm bc. (c) For phase-arm ca. Gray areas highlight overmodulating intervals. Bottom subplot (d) depicts the arm currents.

voltages, in blue for the LC-StatCom and in dashed blue for the conventional CHB StatCom, are shown in Fig. 1(a)–(c). Moreover, the arm currents are shown in Fig. 1(d). In this illustrative example, the capacitor size of the conventional CHB StatCom is four-times larger than the one of the LC-StatCom. As it can be observed, the ac- and dc-side voltages in phase-arms ab and ca are in phase, and thus, large capacitor voltage oscillations do not compromise the converter operation, i.e., no overmodulation occurs. Note that when the dc-side voltage oscillations are in phase with the absolute value of the ac-side voltage, the phase-arm is operating in capacitive mode. On the other hand, the ac- and dc-side voltages in the phase-arm bc are in opposite phase and, therefore, the ability to provide current is restricted, i.e., when the arm current is large enough, overmodulation occurs. Note that when the dc-side voltage oscillations are in counter-phase with the absolute value of the ac-side voltage, the phase-arm is operating in inductive mode. Specifically, in this illustrative example, overmodulation occurs in phase-arm bc of the LC-StatCom during some intervals of the fundamental period, which are highlighted using a gray shading in Fig. 1(b). Unlike the LC-StatCom, the conventional CHB StatCom has a greater capability to provide current in each phase-arm, since the dc-side voltage oscillations are comparably smaller.

Injecting a THZSC in a StatCom adds a degree of freedom in the capacitor voltage references design that can be used to extend the operating limits. Then, the immediate task is finding the physical limits when the optimal THZSC is injected. This is especially beneficial for the LC-StatComs considering their inherent limited negative-sequence current compensation capability [14], as Fig. 1 depicts. A method to extend the limits of positive- and negative-sequence current injection by deriving the optimal THZSC is proposed in this article for balanced and unbalanced grid voltages. Specifically, given an LC-StatCom that is designed to provide a rated positive-sequence current, the proposed method yields the optimal THZSC that corresponds to the theoretical limits of negative-sequence current injection capability of the LC-StatCom.

The benefits and drawbacks of injecting zero-sequence odd harmonics, in different CHB applications, have been reported in [11], [15], [16], [17], [18], [19], and [20]. Capacitor voltage oscillations are neglected in [11], [15], [16], [17], and [18], since large capacitances are considered. On the other hand, capacitor voltage oscillations are considered in [19] and [20], since they use reduced capacitances.

The authors in [15] and [17] focus on star-connected CHB for photovoltaic (PV) applications, assuming balanced grid voltages and currents, and using third-harmonic and discontinuous zero-sequence voltage methods to extend the CHB operation when there are severe PV power generation imbalances among phase-arms. Zhang et al. [11] benchmarked different conventional StatCom solutions for negative-sequence current compensation, such as star- and delta-connected CHBs, and concludes that a THZSC injection represents an effective solution in delta-connected CHB StatComs, whilst a discontinuous zero-sequence voltage is a good solution in star-connected CHB StatComs. Similarly, Lu et al. [18] focused on a conventional star-connected CHB StatCom, and compares a third-harmonic zero-sequence voltage strategy and a square-wave zero-sequence voltage strategy, assuming balanced grid voltages, to show which strategy is more suitable depending on the phase of the negative-sequence current.

The authors in [19] and [20] apply THZSC injection methods to LC-StatCom operating in balanced grid conditions, whereas the proposed approach considers the operating limits when injecting positive- and negative-sequence currents both in balanced and unbalanced grid voltage conditions. It should be noted that injecting negative-sequence currents implies the loss of symmetry among phase-arms due to an unbalanced operation, which complicates the calculation of the required THZSC and, as a result, the determination of the negative-sequence injection capability.

In this article, a linear programming (LP) approach is used to find the optimal THZSC (magnitude and phase) and the maximum negative-sequence current magnitude (for a given phase angle) that the LC-StatCom can inject to the grid for a given capacitor size, while also providing a predetermined amount of positive-sequence current. Therefore, the proposed LP model takes into account the LC-StatCom capacitor voltage oscillations, unbalanced grid voltages, and the FFZSC and THZSC. In the proposed LP method, the dc component of the capacitor voltages in each phase-arm are optimization variables that can enlarge the feasible region while the peak capacitor voltages are constrained. As in [14], which did not consider the THZSC, the operation limits are depicted by straight-line-bounded (polygonal) polar representations. The representation of the operation limits by a polygonal form is an interesting feature of the proposed analysis, since simply knowing the polygon vertices allows one to quickly determine whether the requested operating condition is viable or not. In [14], the polygonal region is derived analytically, however, in the proposed method, due to the presence of the THZSC in the expressions, the polygonal region is obtained by solving an LP problem. It is worth noting that the THZSC injection introduces second- and fourth-harmonics to the original second-harmonic capacitor voltage, and these harmonics do not have to be in phase with the ac-side voltage, which prevents adapting the analytical method in [14]. In addition, an LP approach can include some other constraints, as for instance the limitation of the peak arm current values. Other LP approaches in power electronics can be found, for instance, in [21], [22], and [23].

The rest of this article is organized as follows. In Section II, the modeling of the CHB-StatCom with delta configuration and considering unbalanced grid conditions is reviewed, and the capacitor voltage expressions are derived. Section III models the problem of finding the negative-sequence current limits as an inequality constrained LP. Specifically, two different cases are studied, namely, without THZSC injection and with THZSC. Also, in Section III, straight-line-bounded polar plots are used to represent the viable operating regions in both cases. Section IV deals with the LC-StatCom control used to obtain simulation and experimental results. Section V describes experimental results obtained with a downscaled prototype, where temporal waveforms are shown to corroborate the theoretical results. Finally, Section VI concludes this article.

II. Modeling of LC-StatComs in Presence of Imbalances

The topology of the LC-StatCom with delta configuration, its state variables, and its main mathematical relationships are covered in this section. Imbalances in grid voltages and line currents are taken into account in the model relationships.

A. Topology

Fig. 2 shows a circuit representation of the LC-StatCom with delta configuration. The power converter consists of three phase-arms $x \in \{ab,\ bc,\ ca\}$. Each phase-arm includes n H-bridge converters in cascade, and an arm impedance $\{L_{\text{arm}},\ R_{\text{arm}}\}$.

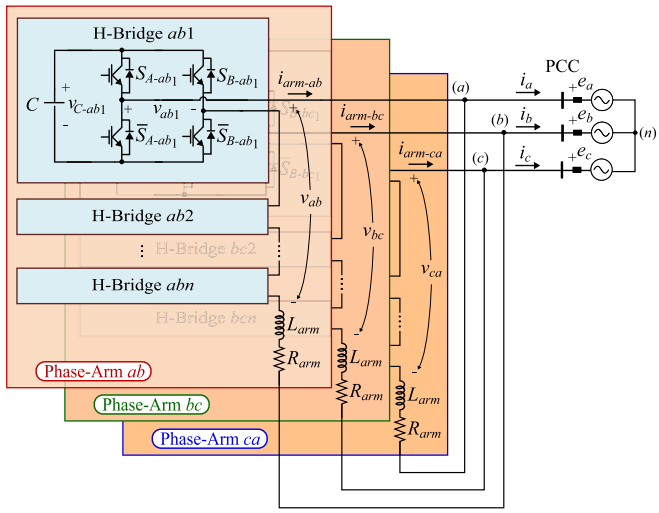

Fig. 2. Circuit diagram of a three-phase CHB StatCom with delta configuration.

Each H-bridge consists of a floating capacitor C, and two pairs of power switches. The three vertices of the delta connection (a), (b), and (c) are connected to the point of common coupling (PCC) grid voltages $\{e_a,\ e_b,\ e_c\}$.

B. Relationships in CHB Converters With Delta Configuration

The capacitor cluster voltages $v_{\Sigma-x}$ are defined as the per-arm sum of individual capacitor voltages, i.e.,

$$v_{\Sigma-x} = \sum_{j=1}^{n} v_{C-xj}. \tag{1}$$

Denoting δ_x as the per-arm modulating signals, which lie in the $[-1,\ 1]$ continuous range, the output voltages v_x correspond to

$$v_x = \delta_x v_{\Sigma-x}. \tag{2}$$

The line currents $\{i_a,\ i_b,\ i_c\}$ are linear combinations of the arm currents $\{i_{\text{arm}-ab},\ i_{\text{arm}-bc},\ i_{\text{arm}-ca}\}$. However, the transformation matrix of line currents to arm currents is nonfull rank until introducing the zero-sequence current i_z as a constraint [24]

$$i_z = \frac{1}{3}\left(i_{\text{arm}-ab} + i_{\text{arm}-bc} + i_{\text{arm}-ca}\right). \tag{3}$$

Then, the following relationship for the converter arm currents can be obtained:

$$\begin{bmatrix} i_{\text{arm}-ab} \\ i_{\text{arm}-bc} \\ i_{\text{arm}-ca} \end{bmatrix} = \frac{1}{3}\begin{bmatrix} 1 & -1 & 0 \\ 0 & 1 & -1 \\ -1 & 0 & 1 \end{bmatrix}\begin{bmatrix} i_a \\ i_b \\ i_c \end{bmatrix} + \begin{bmatrix} 1 \\ 1 \\ 1 \end{bmatrix} i_z. \tag{4}$$

Applying circuit analysis, and using (4), the arm current dynamics are found as

$$\frac{d\, i_{\text{arm}-x}}{dt} = -\frac{R_{\text{arm}}}{L_{\text{arm}}} i_{\text{arm}-x} + \frac{1}{L_{\text{arm}}}\left(v_x - e_x\right) \tag{5}$$

where e_x refers to the line-to-line PCC grid voltages.

The relationship between the ac-side power and the dc-side power in each phase-arm, assuming $v_{C-xj} = v_{\Sigma-x}/n\ \ \forall j \in$

$\{1, 2, \ldots, n\}$, corresponds to

$$\frac{1}{2}\frac{C}{n}\frac{d\,v_{\Sigma-x}^2}{dt} = -v_x i_{\text{arm}-x}. \tag{6}$$

Note that in the steady state, the squared capacitor cluster voltages $v_{\Sigma-x}^2$ consist of a dc value plus a second harmonic, which can be inferred from (5)–(6) when e_x and $i_{\text{arm}-x}$ are sinusoidal. Also note that in steady state, the average power in a grid period T, i.e.,

$$P_{x-\text{avg}} = \frac{1}{T}\int_0^T v_x i_{\text{arm}-x}\,dt \tag{7}$$

can be considered near zero. During transients, $P_{x-\text{avg}}$ can be nonzero which charges/discharges the equivalent arm capacitor C/n.

C. Steady-State Relationships During Unbalances

This subsection models unbalanced operation and provides a coherent set of steady-state references for all the converter variables.

The line-to-line grid voltages and arm currents, in the steady state, can be defined as follows:

$$\begin{aligned}
e_{ab}(t) &= \text{Re}\left(\left(\hat{E}_p + \hat{E}_n e^{-i\theta_n}\right)e^{i\omega t}\right)\\
e_{bc}(t) &= \text{Re}\left(\left(\alpha^2\hat{E}_p + \alpha\hat{E}_n e^{-i\theta_n}\right)e^{i\omega t}\right)\\
e_{ca}(t) &= \text{Re}\left(\left(\alpha\hat{E}_p + \alpha^2\hat{E}_n e^{-i\theta_n}\right)e^{i\omega t}\right)\\
i_{\text{arm}-ab}^{ss}(t) &= \\
&\text{Re}\left(\left(\hat{I}_p^{ss}e^{i\varphi_p^{ss}} + \hat{I}_n^{ss}e^{-i\varphi_n^{ss}} + \hat{I}_{z1}^{ss}e^{i\varphi_{z1}^{ss}}\right)e^{i\omega t}\right)\\
i_{\text{arm}-bc}^{ss}(t) &= \\
&\text{Re}\left(\left(\alpha^2\hat{I}_p^{ss}e^{i\varphi_p^{ss}} + \alpha\hat{I}_n^{ss}e^{-i\varphi_n^{ss}} + \hat{I}_{z1}^{ss}e^{i\varphi_{z1}^{ss}}\right)e^{i\omega t}\right)\\
i_{\text{arm}-ca}^{ss}(t) &= \\
&\text{Re}\left(\left(\alpha\hat{I}_p^{ss}e^{i\varphi_p^{ss}} + \alpha^2\hat{I}_n^{ss}e^{-i\varphi_n^{ss}} + \hat{I}_{z1}^{ss}e^{i\varphi_{z1}^{ss}}\right)e^{i\omega t}\right)
\end{aligned} \tag{8}$$

with phasor rotation operator $\alpha = \exp(i\,2\pi/3)$, subscripts p, n, and z referring to positive-, negative-, and zero-sequence components, respectively, and superscript ss is used for steady-state variables. Parameter ω is the grid angular frequency, $\hat{E}_p$ is the amplitude of the positive-sequence line-to-line grid voltage, $\hat{E}_n$ and θ_n are the amplitude and angle of the negative-sequence line-to-line grid voltage, $\hat{I}_p^{ss}$ and φ_p^{ss} are the amplitude and angle of the positive-sequence arm current, $\hat{I}_n^{ss}$ and φ_n^{ss} are the amplitude and angle of the negative-sequence arm current that the StatCom has to provide, and $\hat{I}_{z1}^{ss}$ and φ_{z1}^{ss} are the amplitude and angle of the FFZSC that impose (7) equal to zero in the steady state, i.e., $P_{x-\text{avg}}^{ss} = 0$. Specifically, the calculation of FFZSC $\{\hat{I}_{z1}^{ss}, \varphi_{z1}^{ss}\}$ is provided in Appendix A. Note that φ_p^{ss} is not necessarily $\pm\pi/2$ rad when dealing with unbalanced grid conditions, as discussed in Appendix A.

Solving (6) according to (34) and (39)–(41) in Appendix A, yields

$$\begin{aligned}
\left(v_{\Sigma-x}^{ss}(t)\right)^2 &= K_x^{ss} + \frac{2E_{xY}I_{xY}^{ss}}{2\omega\,C/n}\sin(2\omega t)\\
&+ \frac{\left(E_{xX} - E_{xY}^2/E_{xX}\right)I_{xY}^{ss}}{2\omega\,C/n}\cos(2\omega t)
\end{aligned} \tag{9}$$

where K_x^{ss} is a design variable that has to be chosen sufficiently large to avoid overmodulation, yet sufficiently low to reduce switching losses [2], [6]. Appendix A describes the mathematical relationships among the voltage and current Cartesian $XY-$components $\{E_{xX}, E_{xY}, I_{xY}^{ss}\}$ and the amplitudes and angles $\{\hat{E}_p, \hat{E}_n, \theta_n, \hat{I}_p^{ss}, \varphi_p^{ss}, \hat{I}_n^{ss}, \varphi_n^{ss}, \hat{I}_{z1}^{ss}, \varphi_{z1}^{ss}\}$ in (8). Note that (38) in Appendix A, which imposes the energy balance among the phase-arms, has been used in (9).

III. Modeling Overmodulation and Overvoltage Constraints in LC-StatComs

Operation of LC-StatComs is limited by the fact that the capacitor cluster voltage $v_{\Sigma-x}^{ss}$ has to be higher than the absolute value of the output voltage $|v_x^{ss}|$, i.e., $|v_x^{ss}| \le v_{\Sigma-x}^{ss}$, otherwise $|\delta_x^{ss}| \ge 1$ according to (2). In addition, $v_{\Sigma-x}^{ss}$ has to be lower than a prescribed maximum value V_{UB}, i.e., $v_{\Sigma-x} \le V_{UB}$, to ensure safe converter operation. The following subsections investigate the maximum negative-sequence current capability of the LC-StatCom by taking into account the capacitor cluster voltage waveform in (9). First, the case with no THZSC is explained, and then a case where a THZSC that extends the operating limits is analyzed. Henceforth, to simplify the equations, the voltage drop on the arm inductor is neglected.

A. Case I: Negative-Sequence Current Capability Without THZSC

As explained, the operating range of the voltage $v_{\Sigma-x}^{ss}$ corresponds to

$$|e_x| \le v_{\Sigma-x}^{ss} \le V_{UB}\;\forall x,\,t. \tag{10}$$

Thus, substituting (34) and (9) in (10), and squaring, yields

$$\begin{aligned}
&\left(E_{xX}\cos(\omega t) + E_{xY}\sin(\omega t)\right)^2 \le K_x^{ss} + \frac{2E_{xY}I_{xY}^{ss}}{2\omega\,C/n}\sin(2\omega t)\\
&+ \frac{\left(E_{xX} - E_{xY}^2/E_{xX}\right)I_{xY}^{ss}}{2\omega\,C/n}\cos(2\omega t) \le V_{UB}^2.
\end{aligned} \tag{11}$$

Now, substituting (39)–(41) in (36), and rearranging, I_{xY}^{ss} can be rewritten as an affine function on the amplitude of the negative-sequence current $\hat{I}_n^{ss}$

$$I_{xY}^{ss} = \alpha_x\hat{I}_n^{ss}\cos(\varphi_n^{ss}) + \beta_x\hat{I}_n^{ss}\sin(\varphi_n^{ss}) + \gamma_x I_{pq}^{ss} \tag{12}$$

where $I_{pq}^{ss} = \hat{I}_p^{ss}\sin(\varphi_p^{ss})$, and where the constants α_x, β_x, and γ_x are solely determined by the grid voltages, i.e, $\hat{E}_p$, $\hat{E}_n$, and θ_n, and therefore they can be regarded as known constants. For instance, for the phase-arm ab current I_{abY}^{ss}, the constants

correspond to

$$\alpha_{ab} = \frac{E_{nq}\left(2E_{nd} - E_{pd}\right)\left(E_{nd} + E_{pd}\right)}{E_{pd}\left(E_{nd}^2 - E_{pd}^2 + E_{nq}^2\right)}$$

$$\beta_{ab} = \frac{\left(E_{nd} + E_{pd}\right)\left(-2E_{pd}^2 + E_{nd}E_{pd} + 2E_{nq}^2\right)}{E_{pd}\left(E_{nd}^2 - E_{pd}^2 + E_{nq}^2\right)}$$

$$\gamma_{ab} = \frac{\left(E_{nd} + E_{pd}\right)\left(E_{pd}^2 - 2E_{nd}E_{pd}\right)}{E_{pd}\left(E_{nd}^2 - E_{pd}^2 + E_{nq}^2\right)}. \tag{13}$$

The six conditions given by (11), two per phase-arm, can be expressed by the following matricial-form inequalities, by replacing (12) into (11):

$$lb_x(t) \leq \begin{bmatrix} a_x\left(t,\, \varphi_n^{ss}\right) & 1 \end{bmatrix} \begin{bmatrix} \hat{I}_n^{ss} \\ K_x^{ss} \end{bmatrix} \leq ub_x(t)$$

$$\forall x,\, t \tag{14}$$

with the lower bounds $lb_x(t)$ and the upper bounds $ub_x(t)$ per phase-arm corresponding to

$$lb_x(t) = \left(E_{xX}\cos\left(\omega t\right) + E_{xY}\sin\left(\omega t\right)\right)^2 - \frac{\gamma_x I_{pq}^{ss}}{2\omega\, C/n}$$
$$\left(2E_{xY}\sin\left(2\omega t\right) + \left(E_{xX} - E_{xY}^2/E_{xX}\right)\cos\left(2\omega t\right)\right) \tag{15}$$

$$ub_x(t) = V_{UB}^2 - \frac{\gamma_x I_{pq}^{ss}}{2\omega\, C/n}$$
$$\left(2E_{xY}\sin\left(2\omega t\right) + \left(E_{xX} - E_{xY}^2/E_{xX}\right)\cos\left(2\omega t\right)\right) \tag{16}$$

being $a_x(t,\, \varphi_n^{ss})$ the coefficient that multiplies the amplitude of the negative-sequence current $\hat{I}_n^{ss}$

$$a_x\left(t,\, \varphi_n^{ss}\right) = \frac{\alpha_x\cos\left(\varphi_n^{ss}\right) + \beta_x\sin\left(\varphi_n^{ss}\right)}{2\omega\, C/n}$$
$$\left(2E_{xY}\sin\left(2\omega t\right) + \left(E_{xX} - E_{xY}^2/E_{xX}\right)\cos\left(2\omega t\right)\right). \tag{17}$$

Note that the variables that are later optimized are the amplitude of the negative-sequence current $\hat{I}_n^{ss}$ and the dc value of the squared capacitor cluster voltages K_x^{ss}.

The lower bounds $lb_x(t)$, upper bounds $ub_x(t)$, and coefficients $a_x(t,\, \varphi_n^{ss})$ in (15)–(17), within $\omega t \in [0,\, \infty]$ rad, are determined by: 1) the grid voltages e_x, which, in turn, allow to obtain the constants α_x, β_x, and γ_x in (13), and the Cartesian $XY-$components $\{E_{xX},\, E_{xY}\}$ in (35), 2) the positive-sequence reactive current reference I_{pq}^{ss}, and 3) the angle of the negative-sequence current φ_n^{ss}. Next, the optimization problem with linear inequalities in (14)–(17) is formulated as an LP, where the optimization variables are $\hat{I}_n^{ss}$, K_{ab}^{ss}, K_{bc}^{ss}, K_{ca}^{ss}, and the cost function is a weighted sum of the optimization variables. The weighted sum aims at maximizing the amplitude of the negative-sequence current, $\hat{I}_n^{ss}$, while the dc value of the squared capacitor cluster voltages, K_{ab}^{ss}, K_{bc}^{ss}, and K_{ca}^{ss}, are desired to be as low as possible. Consequently, the optimization problem with linear objective function and constraints can be expressed as

$$\begin{aligned} &\text{Maximize} \quad \boldsymbol{c}^T\boldsymbol{x} \\ &\text{subject to} \quad \boldsymbol{A}_t\left(t,\, \varphi_n^{ss}\right)\boldsymbol{x} \leq \boldsymbol{b}_t(t),\, \omega t \in [0,\, \infty] \end{aligned} \tag{18}$$

with $[0,\, \infty]$ the infinite index set, and where $\boldsymbol{x} \in \mathbb{R}^4$ is the optimization variable, i.e.,

$$\boldsymbol{x} = \begin{bmatrix} \hat{I}_n^{ss} & K_{ab}^{ss} & K_{bc}^{ss} & K_{ca}^{ss} \end{bmatrix}^T. \tag{19}$$

Vector $\boldsymbol{c}$ defines the cost function $\boldsymbol{c}^T\boldsymbol{x}$, as

$$\boldsymbol{c} = \begin{bmatrix} 1 & -\rho & -\rho & -\rho \end{bmatrix}^T \tag{20}$$

where $\rho > 0$ is a positive constant. Matrix $\boldsymbol{A}_t$ and vector $\boldsymbol{b}_t$ define the inequality constraints

$$\boldsymbol{A}_t\left(t,\, \varphi_n^{ss}\right) = \begin{bmatrix} a_{ab}\left(t,\, \varphi_n^{ss}\right) & 1 & 0 & 0 \\ a_{bc}\left(t,\, \varphi_n^{ss}\right) & 0 & 1 & 0 \\ a_{ca}\left(t,\, \varphi_n^{ss}\right) & 0 & 0 & 1 \\ -a_{ab}\left(t,\, \varphi_n^{ss}\right) & -1 & 0 & 0 \\ -a_{bc}\left(t,\, \varphi_n^{ss}\right) & 0 & -1 & 0 \\ -a_{ca}\left(t,\, \varphi_n^{ss}\right) & 0 & 0 & -1 \\ -1 & 0 & 0 & 0 \\ 0 & -1 & 0 & 0 \\ 0 & 0 & -1 & 0 \\ 0 & 0 & 0 & -1 \end{bmatrix} \tag{21}$$

$$\boldsymbol{b}_t(t) = \begin{bmatrix} ub_{ab}(t) \\ ub_{bc}(t) \\ ub_{ca}(t) \\ -lb_{ab}(t) \\ -lb_{bc}(t) \\ -lb_{ca}(t) \\ 0 \\ 0 \\ 0 \\ 0 \end{bmatrix} \tag{22}$$

where the first six rows in (21) and (22) correspond to (14), while the last four rows impose that the optimization variables $\hat{I}_n^{ss}$, K_{ab}^{ss}, K_{bc}^{ss}, K_{ca}^{ss} are positive.

As it can be observed, there is a finite number of variables to optimize, i.e., $\hat{I}_n^{ss}$, K_{ab}^{ss}, K_{bc}^{ss}, K_{ca}^{ss}. Conversely, there exists a constraint for each $t \in [0,\, \infty]$, thus, the number of constraints are infinite. Hence, (18) is a linear semiinfinite optimization problem [25]. However, since only sinusoidal signals with periodicity equal to $T/2$ are involved in the coefficients of $\boldsymbol{A}_t$ and $\boldsymbol{b}_t$, according to (15)–(17), the infinite index set of interest is $t \in [0,\, T/2]$. Discretization, using N_s uniformly sampled values within $T/2$, of (15)–(17), within the index set $t \in [0,\, T/2]$, or equivalently $\omega t \in [0,\, \pi]$, transforms the semiinfinite optimization problem into a finite-dimension LP problem [26]. Note that

the incorporation of additional constraints in the LP problem, such as limiting the maximum arm currents, can be readily implemented.

After discretizing (21) and (22) with N_s samples along $T/2$, (18) becomes the following inequality form LP:

$$\begin{array}{ll} \text{Maximize} & \boldsymbol{c}^T \boldsymbol{x} \\ \text{subject to} & \boldsymbol{A}\left(\varphi_n^{ss}\right) \boldsymbol{x} \leq \boldsymbol{b} \end{array} \tag{23}$$

with the new time-invariant matrix $\boldsymbol{A}$ and vector $\boldsymbol{b}$ defining the linear constraints as

$$\boldsymbol{A}\left(\varphi_n^{ss}\right) = \begin{bmatrix} \boldsymbol{a}_{ab}\left(\varphi_n^{ss}\right) & \mathbf{1}_{N_s} & \mathbf{0}_{N_s} & \mathbf{0}_{N_s} \\ \boldsymbol{a}_{bc}\left(\varphi_n^{ss}\right) & \mathbf{0}_{N_s} & \mathbf{1}_{N_s} & \mathbf{0}_{N_s} \\ \boldsymbol{a}_{ca}\left(\varphi_n^{ss}\right) & \mathbf{0}_{N_s} & \mathbf{0}_{N_s} & \mathbf{1}_{N_s} \\ -\boldsymbol{a}_{ab}\left(\varphi_n^{ss}\right) & -\mathbf{1}_{N_s} & \mathbf{0}_{N_s} & \mathbf{0}_{N_s} \\ -\boldsymbol{a}_{bc}\left(\varphi_n^{ss}\right) & \mathbf{0}_{N_s} & -\mathbf{1}_{N_s} & \mathbf{0}_{N_s} \\ -\boldsymbol{a}_{ca}\left(\varphi_n^{ss}\right) & \mathbf{0}_{N_s} & \mathbf{0}_{N_s} & -\mathbf{1}_{N_s} \\ -1 & 0 & 0 & 0 \\ 0 & -1 & 0 & 0 \\ 0 & 0 & -1 & 0 \\ 0 & 0 & 0 & -1 \end{bmatrix} \tag{24}$$

$$\boldsymbol{b} = \begin{bmatrix} \boldsymbol{ub}_{ab} \\ \boldsymbol{ub}_{bc} \\ \boldsymbol{ub}_{ca} \\ -\boldsymbol{lb}_{ab} \\ -\boldsymbol{lb}_{bc} \\ -\boldsymbol{lb}_{ca} \\ 0 \\ 0 \\ 0 \\ 0 \end{bmatrix} \tag{25}$$

with $\mathbf{1}_{N_s}$ and $\mathbf{0}_{N_s}$ as N_s-size column vectors of ones and zeros, respectively. Column vector $\boldsymbol{a}_x(\varphi_n^{ss})$ in (24) is defined as

$$\boldsymbol{a}_x = \begin{bmatrix} a_x(0) \\ a_x\left(T_s\right) \\ a_x\left(2T_s\right) \\ \vdots \\ a_x\left(\eta T_s\right) \\ \vdots \\ a_x\left(\left(N_s-1\right)T_s\right) \end{bmatrix} \tag{26}$$

with $a_x(\eta T_s)$ as the value of (17) at $\omega t = \pi\eta/N_s$, $\eta \in \{0, 1, \ldots, N_s - 1\}$ being the sample index. The column vectors $\boldsymbol{lb}_x$ and $\boldsymbol{ub}_x$ in (25) are similarly calculated. Note that now the discretized constraints set is modeled by the LP matrices $\boldsymbol{A}(\varphi_n^{ss}) \in \mathbb{R}^{(6N_s+4)\times 4}$ and $\boldsymbol{b} \in \mathbb{R}^{(6N_s+4)}$, which have a finite dimension. Inequalities $\boldsymbol{A}(\varphi_n^{ss})\boldsymbol{x} \leq \boldsymbol{b}$ consider both balanced and unbalanced grid voltage conditions, depending on the particular values of E_{pd}, E_{nd}, and E_{nq} in constants α_x, β_x, and γ_x in (13).

B. Case II: Negative-Sequence Current Capability With THZSC

Injecting a THZSC can extend the operating region. Note that the THZSC does not affect the active power balance, i.e., (39)–(41) in Appendix A are unchanged. It can be remarked that the THZSC modifies the shape of the cluster capacitor voltage waveforms $v_{\Sigma-x}^{ss}$ in (9), and hence the modulation signals δ_x^{ss} according to (2). Next, the analysis including the THZSC is described.

Considering the THZSC, the arm currents in (34) can be expressed as follows:

$$\begin{aligned} i_{\text{arm}-x}^{ss}(t) = {} & I_{xX}^{ss}\cos\left(\omega t\right) + I_{xY}^{ss}\sin\left(\omega t\right) \\ & + I_{z3X}^{ss}\cos\left(3\omega t\right) + I_{z3Y}^{ss}\sin\left(3\omega t\right) \end{aligned} \tag{27}$$

and consequently, the shaped cluster capacitor voltages become

$$\begin{aligned} \left(v_{\Sigma-x}^{ss}(t)\right)^2 = {} & K_x^{ss} + \frac{2E_{xY}I_{xY}^{ss}}{2\omega\, C/n}\sin\left(2\omega t\right) \\ & + \frac{\left(E_{xX} - E_{xY}^2/E_{xX}\right)I_{xY}^{ss}}{2\omega\, C/n}\cos\left(2\omega t\right) \\ & - \frac{E_{xX}I_{z3X}^{ss} + E_{xY}I_{z3Y}^{ss}}{2\omega\, C/n}\sin\left(2\omega t\right) \\ & - \frac{E_{xX}I_{z3X}^{ss} - E_{xY}I_{z3Y}^{ss}}{4\omega\, C/n}\sin\left(4\omega t\right) \\ & + \frac{E_{xX}I_{z3Y}^{ss} - E_{xY}I_{z3X}^{ss}}{2\omega\, C/n}\cos\left(2\omega t\right) \\ & + \frac{E_{xX}I_{z3Y}^{ss} + E_{xY}I_{z3X}^{ss}}{4\omega\, C/n}\cos\left(4\omega t\right). \end{aligned} \tag{28}$$

Comparing (9) with (28), the THZSC adds two extra harmonic components to $v_{\Sigma-x}^{ss\,2}$, namely, a second- and a fourth-harmonic term. It can be seen that, since $E_{abX} \neq E_{bcX} \neq E_{caX}$ and $E_{abY} \neq E_{bcY} \neq E_{caY}$ in (35), the effect of the extra terms due to the THZSC in the three converter phase-arms is asymmetric.

Satisfying the constraint (10), where $v_{\Sigma-x}^{ss}$ in (28) and e_x are neither in phase nor in counter-phase, and, given the presence of several harmonics in (28), it involves that the constraint (10) is not independent on the time instant t. Nevertheless, the proposed LP method deals properly with the aforementioned time-dependent constraint.

As in the previous case, the dc value of the squared capacitor cluster voltages, i.e., K_{ab}^{ss}, K_{bc}^{ss}, K_{ca}^{ss}, are considered as optimization variables. Thus, the optimization vector $\boldsymbol{x} \in \mathbb{R}^6$, in this case, becomes

$$\boldsymbol{x} = \begin{bmatrix} \hat{I}_n^{ss} & K_{ab}^{ss} & K_{bc}^{ss} & K_{ca}^{ss} & I_{z3X}^{ss} & I_{z3Y}^{ss} \end{bmatrix}^T \tag{29}$$

the vector $\boldsymbol{c}$ that defines the linear cost function is now

$$\boldsymbol{c} = \begin{bmatrix} 1 & -\rho & -\rho & -\rho & 0 & 0 \end{bmatrix}^T \tag{30}$$

and the matrix $\boldsymbol{A}$, which models the linear constraints $\boldsymbol{A}(\varphi_n^{ss})\boldsymbol{x} \leq \boldsymbol{b}$, now corresponds to

$$\boldsymbol{A}\left(\varphi_n^{ss}\right) = \begin{bmatrix} \boldsymbol{a}_{ab}\left(\varphi_n^{ss}\right) & \mathbf{1}_{N_s} & \mathbf{0}_{N_s} & \mathbf{0}_{N_s} & \boldsymbol{q}_{abX} & \boldsymbol{q}_{abY} \\ \boldsymbol{a}_{bc}\left(\varphi_n^{ss}\right) & \mathbf{0}_{N_s} & \mathbf{1}_{N_s} & \mathbf{0}_{N_s} & \boldsymbol{q}_{bcX} & \boldsymbol{q}_{bcY} \\ \boldsymbol{a}_{ca}\left(\varphi_n^{ss}\right) & \mathbf{0}_{N_s} & \mathbf{0}_{N_s} & \mathbf{1}_{N_s} & \boldsymbol{q}_{caX} & \boldsymbol{q}_{caY} \\ -\boldsymbol{a}_{ab}\left(\varphi_n^{ss}\right) & -\mathbf{1}_{N_s} & \mathbf{0}_{N_s} & \mathbf{0}_{N_s} & -\boldsymbol{q}_{abX} & -\boldsymbol{q}_{abY} \\ -\boldsymbol{a}_{bc}\left(\varphi_n^{ss}\right) & \mathbf{0}_{N_s} & -\mathbf{1}_{N_s} & \mathbf{0}_{N_s} & -\boldsymbol{q}_{bcX} & -\boldsymbol{q}_{bcY} \\ -\boldsymbol{a}_{ca}\left(\varphi_n^{ss}\right) & \mathbf{0}_{N_s} & \mathbf{0}_{N_s} & -\mathbf{1}_{N_s} & -\boldsymbol{q}_{caX} & -\boldsymbol{q}_{caY} \\ -1 & 0 & 0 & 0 & 0 & 0 \\ 0 & -1 & 0 & 0 & 0 & 0 \\ 0 & 0 & -1 & 0 & 0 & 0 \\ 0 & 0 & 0 & -1 & 0 & 0 \end{bmatrix} \tag{31}$$

where $\boldsymbol{q}_{xX}$ and $\boldsymbol{q}_{xY}$ are N_s-size column vectors, where, as in the previous case, N_s corresponds to the samples along $T/2$. That is, each coordinate $q_{xX}(\eta T_s)$ and $q_{xY}(\eta T_s)$, η being $\eta \in \{0, 1, \ldots, N_s - 1\}$, according to (28), correspond to

$$\begin{aligned} & q_{xX}\left(\eta T_s\right) \\ &= -\frac{E_{xX}}{2\omega\, C/n}\sin\left(2\pi\eta/N_s\right) - \frac{E_{xX}}{4\omega\, C/n}\sin\left(4\pi\eta/N_s\right) \\ &\quad - \frac{E_{xY}}{2\omega\, C/n}\cos\left(2\pi\eta/N_s\right) + \frac{E_{xY}}{4\omega\, C/n}\cos\left(4\pi\eta/N_s\right) \end{aligned} \tag{32}$$

$$\begin{aligned} & q_{xY}\left(\eta T_s\right) \\ &= -\frac{E_{xY}}{2\omega\, C/n}\sin\left(2\pi\eta/N_s\right) + \frac{E_{xY}}{4\omega\, C/n}\sin\left(4\pi\eta/N_s\right) \\ &\quad + \frac{E_{xX}}{2\omega\, C/n}\cos\left(2\pi\eta/N_s\right) + \frac{E_{xX}}{4\omega\, C/n}\cos\left(4\pi\eta/N_s\right). \end{aligned} \tag{33}$$

Note that vector $\boldsymbol{b}$ does not change with respect to (25). Therefore, now, the LP matrices with THZSC injection have dimension $\boldsymbol{A}(\varphi_n^{ss}) \in \mathbb{R}^{(6N_s+4)\times 6}$ and $\boldsymbol{b} \in \mathbb{R}^{(6N_s+4)}$.

The feasible operating regions are then obtained, for a given set of $\{E_{pd}, E_{nd}, E_{nq}, C, I_{pq}^{ss}, \varphi_n^{ss}\}$, by solving the proposed LP problem (23) in MATLAB (`X = linprog(f,A,b)`). In this way, the LP outputs, i.e., 1) a polygonal region in polar coordinates with $\hat{I}_n^{ss}$ and φ_n^{ss} as axes, as described in [14], for the case without THZSC, which delimits the feasible operating range, 2) the optimal dc value of the squared capacitor cluster voltages K_{ab}^{ss}, K_{bc}^{ss}, K_{ca}^{ss}, and 3) the optimal THZSC components I_{z3X}^{ss}, I_{z3Y}^{ss}, are obtained. Note that the obtained values can be used as the steady-state references for the controller, as discussed in Section IV. A more detailed explanation of the previous procedural steps is explained in Appendix B.

For the purpose of illustrating the extended operating region due to the THZSC injection, two simulation examples are provided next. *Example B1* considers balanced grid voltages, while *Example B*2 considers an unbalanced grid voltage condition. Both examples consider a 36-MVA StatCom with five submodules per phase-arm connected to a 6-kV rms line-to-neutral grid. A phase-shifted carrier pulsewidth modulation (PSC-PWM) strategy with 2-kHz carriers has been adopted. The system is simulated in MATLAB/Simulink environment. The system parameters are given in Table I, where the capacitor size is small enough such that the StatCom can be considered an LC-StatCom [2]. To make the operational limits independent of the rated arm current $\hat{I}_R$, the limits are expressed according to the requested positive-sequence reactive current ratio, namely, $\lambda_{pq}^{ss} = I_{pq}^{ss}/\hat{I}_R$, and the negative-sequence compensation ratio, namely, $\lambda_n^{ss} = \hat{I}_n^{ss}/\hat{I}_R$. The following illustrative examples consider a given $\lambda_{pq}^{ss} = -0.5$ (the StatCom is injecting 50%-rated positive-sequence reactive current).

TABLE I
SIMULATION PARAMETERS

Parameter	Value
Rated line-to-line grid voltage amplitude, $\hat{E}_R$	$6\sqrt{2}\sqrt{3}$ kV (1 p.u.)
Number of H-bridge submodules per phase-arm, n	5
Rated grid power, S_R	36 MVA (1 p.u.)
Rated arm current amplitude, $\hat{I}_R$	$2\sqrt{2/3}$ kA (1 p.u.)
Grid angular frequency, ω_g	100π rad/s
Upper bound capacitor voltage, V_{UB}	$1.3\hat{E}_R/n = 3.82$ kV
Capacitance per H-bridge, C	1.43 mF (0.27 p.u.)
Filter inductances, L_{arm}	0.72 mH (0.03 p.u.)
Carrier frequency, f_c	2 kHz

1) Example B1: Fig. 3(a) depicts the negative-sequence current injection region, indicated using shaded orange. It is worth noting that the negative-sequence current deliverable region is defined by two distinct sets of straight lines: a black border and a magenta border. The operating region with a black border represents the case without THZSC [14], whereas the magenta border represents the enlarged operating region by the optimal THZSC injection calculated using the proposed LP procedure. The enlargement of the polygonal area represents an enhancement in the capability of delivering negative-sequence current due to the optimal THZCS.

Coordinate values $(\lambda_n^{ss}, \varphi_n^{ss})$, indicated by crosses "×" in Fig. 3(a), correspond to: ① $(0, 5\pi/6)$, ②$(0.25, 5\pi/6)$, ③ $(0.50, 5\pi/6)$, ④ $(0.65, 5\pi/6)$. The transitions between ①, ②, ③, and ④ occur at time instants 0.05, 0.15, and 0.25 s, respectively, and the corresponding time-domain waveforms are shown in Fig. 3. Note that ①, ②, and ③ are all located within the orange polygonal area bounded by the black border in Fig. 3(a), while coordinate ④ is outside of it, and thus, the LC-StatCom without THZSC will overmodulate and fail to provide the required current. The coordinate ④ is, however, within the enlarged polygonal area bounded by the magenta lines, which, as previously stated, represents the limits with the inclusion of the THZSC, and thus the LC-StatCom with the proposed optimal THZSC will not overmodulate.

As it can be seen in Fig. 3(b)–(d), the capacitor cluster voltages $v_{\Sigma-x}$ are always well above the corresponding absolute values of the ac-side voltages $|e_x|$ in ①and ②, whereas in ③, the minimum of $v_{\Sigma-bc}$ is close to the maximum of $|e_{bc}|$, which corroborates that ③ is near the limit of the black-bordered polygonal bound

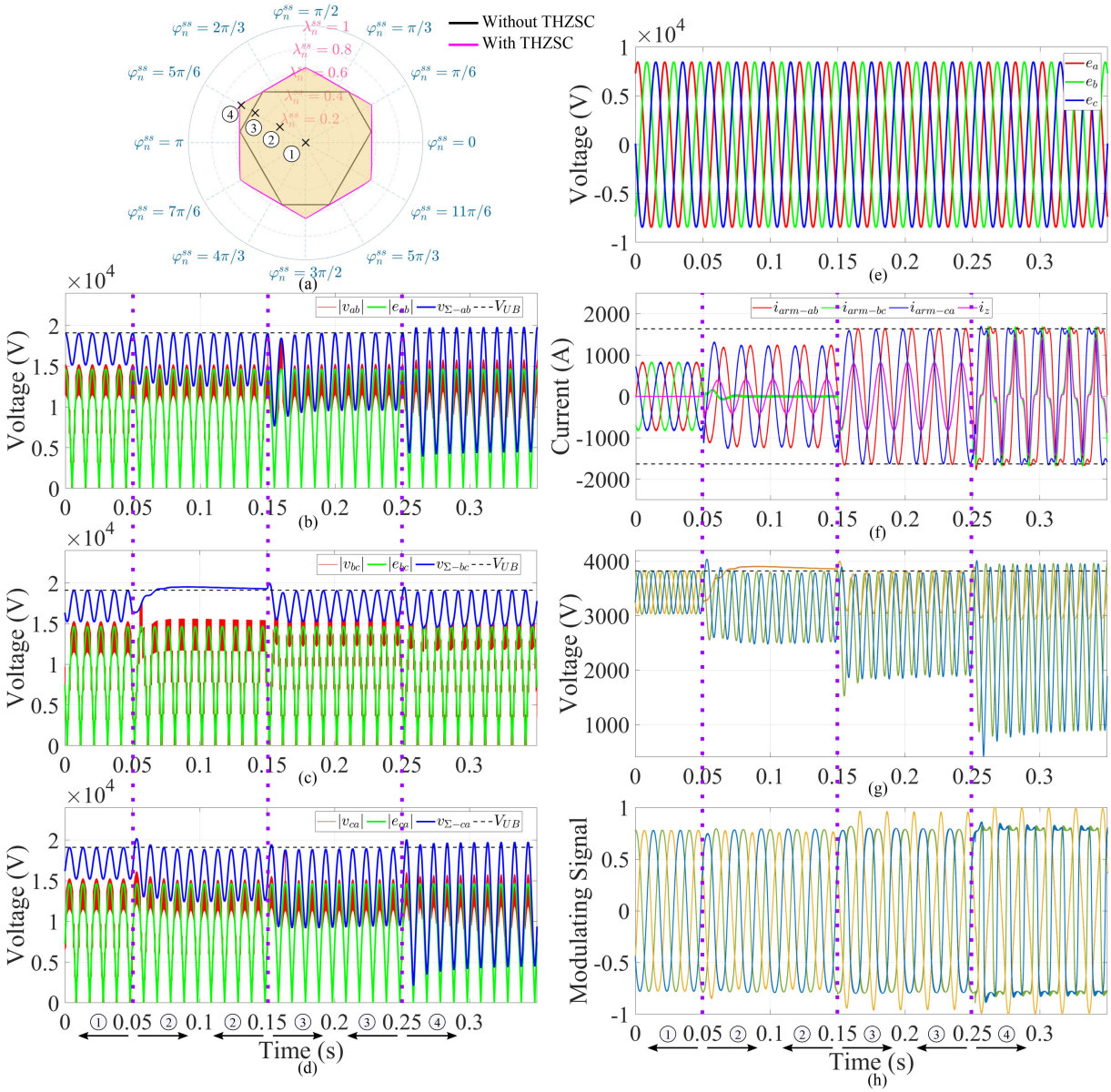

Fig. 3. *Example B1* simulation waveforms when the LC-StatCom is operating with balanced grid voltages and providing half of the rated positive-sequence reactive current $\lambda_{pq}^{ss} = -0.5$, while delivering a negative-sequence current with normalized amplitude λ_n^{ss} and phase-angle φ_n^{ss} for four different value sets $(\lambda_n^{ss}, \varphi_n^{ss})$: ①$(0, 5\pi/6)$, ②$(0.25, 5\pi/6)$, ③$(0.50, 5\pi/6)$, and ④$(0.65, 5\pi/6)$. (a) Operating ranges (in magenta with THZSC and in black without THZSC) of the LC-StatCom, (b) phase-arm ab voltages v_{ab}, $v_{\Sigma-ab}$, (c) phase-arm bc voltages v_{bc}, $v_{\Sigma-bc}$, (d) phase-arm ca voltages v_{ca}, $v_{\Sigma-ca}$, (e) line-to-neutral grid voltages, (f) arm currents $i_{\text{arm}-x}$, (g) capacitor voltages v_{C-xj} (15 signals), and (h) submodule modulating signals (15 signals).

(without THZSC). In ④, the proposed THZSC is injected, as it can be seen in the arm current waveforms in Fig. 3(f). It is important to remark that this THZSC does not appear in the line currents. As expected, the optimal THZSC injection shapes $v_{\Sigma-bc}$ such that it is always above $|e_{bc}|$ while operating at ④, thus preventing the occurrence of overmodulation, as shown in Fig. 3(c) shows. Also, it can be observed in Fig. 3(h) that all the submodule modulating signals are within $[-1, 1]$ range, and all the submodule capacitor voltages in Fig. 3(h) are well balanced. These facts corroborate that the proposed THZSC enhances the capability of providing negative-sequence current.

2) Example B2: This example considers the same LC-StatCom configuration and parameters of *Example B*1, given in Table I, for an unbalanced grid condition where the line-to-neutral voltage in phase a is 50% below the nominal value and the rest of phases have nominal voltage. Fig. 4(e) shows this grid voltage condition.

Similar to the previous example, the operating negative-sequence coordinates correspond to: ① $(0, 5\pi/6)$, ② $(0.2, 5\pi/6)$, ③$(0.4, 5\pi/6)$, which are inside the black-bordered polygonal area, and ④ $(0.65, 5\pi/6)$ that is outside of it but within the magenta-bordered polygonal area. A similar behavior is observed in terms of the voltages in Fig. 4(b)–(d),

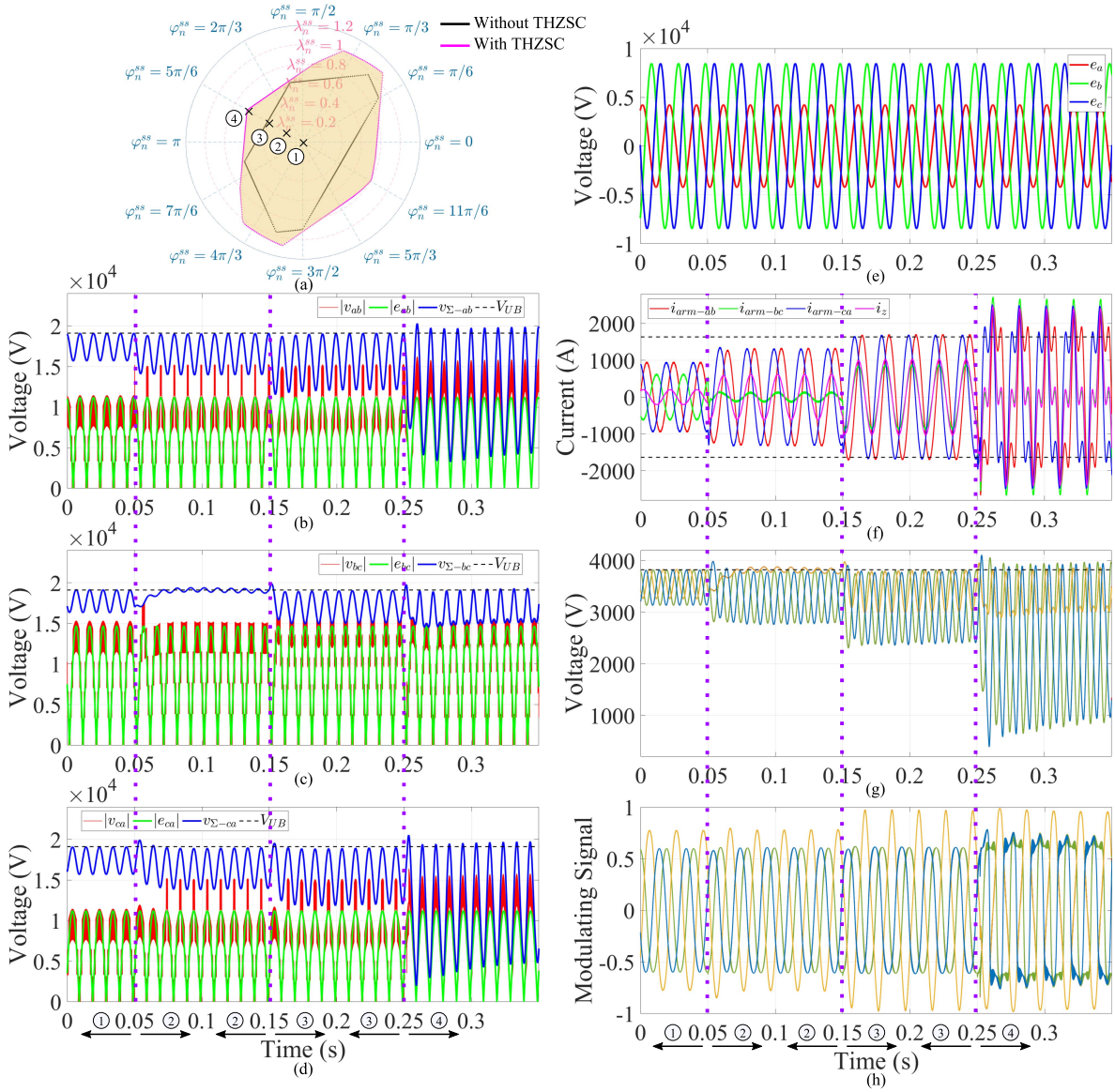

Fig. 4. *Example B*2 simulation waveforms when the LC-StatCom is operating with unbalanced grid voltages and providing half of the rated positive-sequence reactive current $\lambda_{pq}^{ss} = -0.5$, while delivering a negative-sequence current with normalized amplitude λ_n^{ss} and phase-angle φ_n^{ss} for four different value sets $(\lambda_n^{ss}, \varphi_n^{ss})$: ①$(0, 5\pi/6)$, ②$(0.20, 5\pi/6)$, ③$(0.40, 5\pi/6)$, ④$(0.65, 5\pi/6)$. (a) Operating ranges (in magenta with THZSC and in black without THZSC) of the LC-StatCom, (b) phase-arm ab voltages v_{ab}, $v_{\Sigma-ab}$, (c) phase-arm bc voltages v_{bc}, $v_{\Sigma-bc}$, (d) phase-arm ca voltages v_{ca}, $v_{\Sigma-ca}$, (e) line-to-neutral grid voltages, (f) arm currents $i_{\text{arm}-x}$, (g) capacitor voltages v_{C-xj} (15 signals), and (h) submodule modulating signals (15 signals).

namely, Fig. 4(c) shows that the phase-arm bc transits from a capacitive behavior (that is when $v_{\Sigma-bc}$ and $|e_{bc}|$ are in phase) to an inductive behavior (that is when $v_{\Sigma-bc}$ and $|e_{bc}|$ are in quadrature) as λ_n^{ss} increases, while the phase-arms ab and ca maintain their capacitive behavior during this simulation interval, as Fig. 4(b) and (d) illustrate. With the inclusion of the proposed optimal THZSC, the LC-StatCom can provide the requested negative-sequence current with parameters $\lambda_n^{ss} = 0.65$ and $\varphi_n^{ss} = 5\pi/6$ rad without overmodulation. This result shows that the proposed THZSC enhances the capability of providing negative-sequence current by 55% approximately for this specific angle of the negative-sequence current component. Again, it can seen that while operating at ④, the arm currents in Fig. 4(f) show a third-harmonic component in addition to the fundamental component. Furthermore, all the submodule capacitor voltages are always well balanced, as Fig. 4(g) shows, and all the submodule modulating signals are within $[-1, 1]$ range, as depicted in Fig. 4(h).

The black-bordered polygonal area in Fig. 4(a) that limits the negative-sequence current capability for the unbalanced grid voltage case shows only one axis of symmetry, whereas the balanced grid voltage case in Fig. 3(a) shows three axes of symmetry. The injection of the proposed THZSC not only expands the polygonal areas but it also doubles their axes of symmetry.

3) Benchmark: Fig. 5 shows the influence of the capacitor size on the orange polygonal areas depicted in Fig. 3(a). It can be seen that for the chosen capacitor size, $C = 1.43$ mF, the

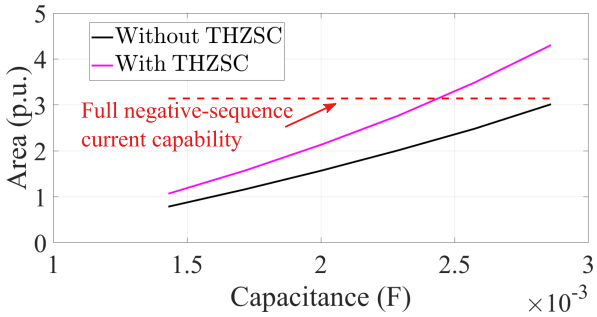

Fig. 5. Capacitance value influence in the negative-sequence current compensation area (in magenta with THZSC and in black without THZSC), for balanced grid voltages and $\lambda_{pq}^{ss} = -0.5$.

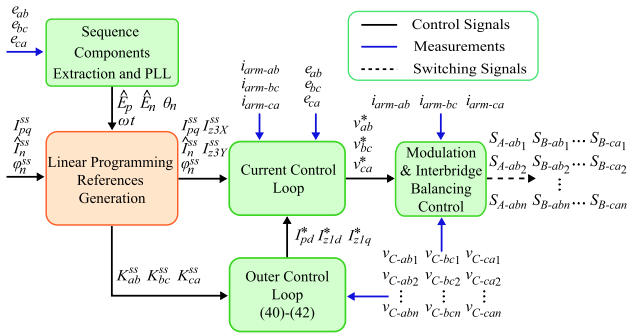

Fig. 6. Control block diagram.

black-bordered compensating area (without THZSC) is 0.25π. After injecting the proposed THZSC, the area increases to 0.34π, which represents a 36% increase. Also note that if a total area of π is desired, which means that the StatCom has full negative-sequence current capability, i.e., it can operate anywhere in the unit circle of the polar plot, a 2.2 times larger capacitance is needed without THZSC, whereas only a 1.7 times larger capacitance is needed if injecting the proposed THZSC.

As it can be observed in Figs. 3(g) and 4(g), the dc component of the capacitor voltages is reduced with respect to a conventional StatCom solution (with a capacitor size large enough to neglect the capacitor voltage oscillations). This involves lower averaged blocking voltage in the switching semiconductors and consequently lower averaged switching power loss [3]. Comparing the proposed solution with a conventional StatCom at operating point ④ of Fig. 3(a), 27 % reduction in the averaged switching loss power is expected (assuming identical switching semiconductor). On the other hand, the averaged conduction loss power would increase slightly due to the THZSC injection. Specifically, comparing the proposed solution with a conventional StatCom at operating point ④, the averaged conduction loss power is expected to increase by 4.5 %.

As mentioned, the THZSC injection is not seen in the line currents $\{i_a, i_b, i_c\}$. Comparing the proposed solution with a conventional StatCom at operating point ④ of Fig. 3(a), 154 % improvement is observed in the total harmonic distortion (THD) value of the line current with the largest amplitude (line current i_a in *Example B1*), while THD improvements of more than 50 % are obtained in the line currents with smaller amplitudes (line currents i_b and i_c in *Example B1*).

IV. LC-StatCom Control

This section provides the details of the LC-StatCom control system implemented in prototypes in order to validate the proposed approach in simulation and experimental results.

The controller, that is shown in Fig. 6, has a conventional cascaded-loop structure. First, the block named "Sequence Components Extraction and PLL" extracts the positive- and negative-sequence components $\{\hat{E}_p, \hat{E}_n, \theta_n\}$ of the line-to-line grid voltages $\{e_{ab}, e_{bc}, e_{ca}\}$ by using the Fortescue's transformation and dq rotation transformations. Moreover, a PLL uses the extracted positive-sequence grid voltage to calculate the angle ωt for synchronization. Second, the block named "Linear Programming References Generation" provides the steady-state references according to Section III, specifically using (23). Note that this "Linear Programming References Generation" block is highlighted using a different color in Fig. 6. The inputs to the "Linear Programming References Generation" block are 1) the desired positive-sequence reactive current I_{pq}^{ss} and the desired negative-sequence current $\{\hat{I}_n^{ss}, \varphi_n^{ss}\}$, and 2) the measured grid voltage condition $\{\hat{E}_p, \hat{E}_n, \theta_n\}$, whereas

TABLE II
Experimental System Parameters

Parameter	Value
Rated line-to-line grid voltage amplitude, $\hat{E}_R$	$60\sqrt{2}\sqrt{3}$ V (1 p.u.)
Number of H-bridge submodules per phase-arm, n	2
Rated grid power, S_R	2 kVA (1 p.u.)
Rated arm current amplitude, $\hat{I}_R$	$11\sqrt{2/3}$ A (1 p.u.)
Grid angular frequency, ω_g	100π rad/s
Upper bound capacitor voltage, V_{UB}	$1.3\hat{E}_R/n = 95.5$ V
Capacitance per H-bridge, C	300 μF (0.26 p.u.)
Filter inductances, L_{arm}	2 mH (0.04 p.u.)
Carrier frequency, f_c	10 kHz

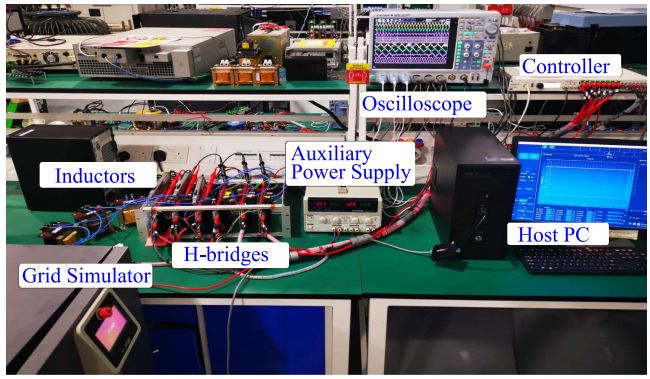

Fig. 7. Experimental setup.

Fig. 8. Experimental waveforms for different negative-sequence current injections corresponding to ①, ②, ③, ④, for balanced grid voltages, and $\lambda_{pq}^{ss} = -0.5$. Left column: Without optimal THZSC injection. Right column: With optimal THZSC injection. Channels CH1, 2, and 3 show the PWM converter voltages v_x, and Channels CH4, 5, and 6 show the arm currents $i_{\text{arm}-x}$.

the outputs are a) the optimal dc values of the squared capacitor cluster voltages $\{K_{ab}^{ss}, K_{bc}^{ss}, K_{ca}^{ss}\}$, and b) the optimal THZSC components $\{I_{z3X}^{ss}, I_{z3Y}^{ss}\}$, which have been obtained from the proposed LP approach.

Next, the "Outer Control Loop" block calculates the FFZSC amplitude and angle $\{\hat{I}_{z1}^{*}, \varphi_{z1}^{*}\}$, and the positive-sequence active current I_{pd}^{*}, which maintain the cluster capacitor voltages tightly controlled among the CHB phase-arms. Specifically, the "Outer Control Loop" block uses three proportional–integral (PI) controllers to steer the measured values $\{K_{ab}, K_{bc}, K_{ca}\}$ toward their desired steady-state values $\{K_{ab}^{ss}, K_{bc}^{ss}, K_{ca}^{ss}\}$. The PI-outputs correspond to the averaged phase-arm powers $\{P_{ab-\text{avg}}^{*}, P_{bc-\text{avg}}^{*}, P_{ca-\text{avg}}^{*}\}$, which are then mapped to $\{I_{z1d}^{*}, I_{z1q}^{*}, I_{pd}^{*}\}$ using the linear transformation (42). Note that the relationship between amplitude and angle $\{\hat{I}_{z1}^{*}, \varphi_{z1}^{*}\}$ and its corresponding $dq-$components $\{I_{z1d}^{*}, I_{z1q}^{*}\}$ is $I_{z1d}^{*} = \hat{I}_{z1}^{*}\cos(\varphi_{z1}^{*})$, $I_{z1q}^{*} = \hat{I}_{z1}^{*}\sin(\varphi_{z1}^{*})$. Values $\{K_{ab}, K_{bc}, K_{ca}\}$ are extracted using second-order generalized-integrator (SOGI) filters. Combining the static current references $\{I_{pq}^{ss}, \hat{I}_{n}^{ss}, \varphi_{n}^{ss}, I_{z3X}^{ss}, I_{z3Y}^{ss}\}$ with the "Outer Control Loop" block outputs $\{I_{z1d}^{*}, I_{z1q}^{*}, I_{pd}^{*}\}$, the arm current references $\{i_{\text{arm}-ab}^{*}, i_{\text{arm}-bc}^{*}, i_{\text{arm}-ca}^{*}\}$ are obtained. The "Current Control Loop" block provides the output voltage references $\{v_{ab}^{*}, v_{bc}^{*}, v_{ca}^{*}\}$ by processing the errors between measured arm currents $i_{\text{arm}-x}$ and references $i_{\text{arm}-x}^{*}$. The implemented "Current Control Loop" uses a state feedback approach [27]. Then, $\{v_{ab}^{*}, v_{bc}^{*}, v_{ca}^{*}\}$ constitute the input of the block "Modulation & Interbridge Balancing Control," which, in turn, generates appropriate signals for the switches using a PSC-PWM method.

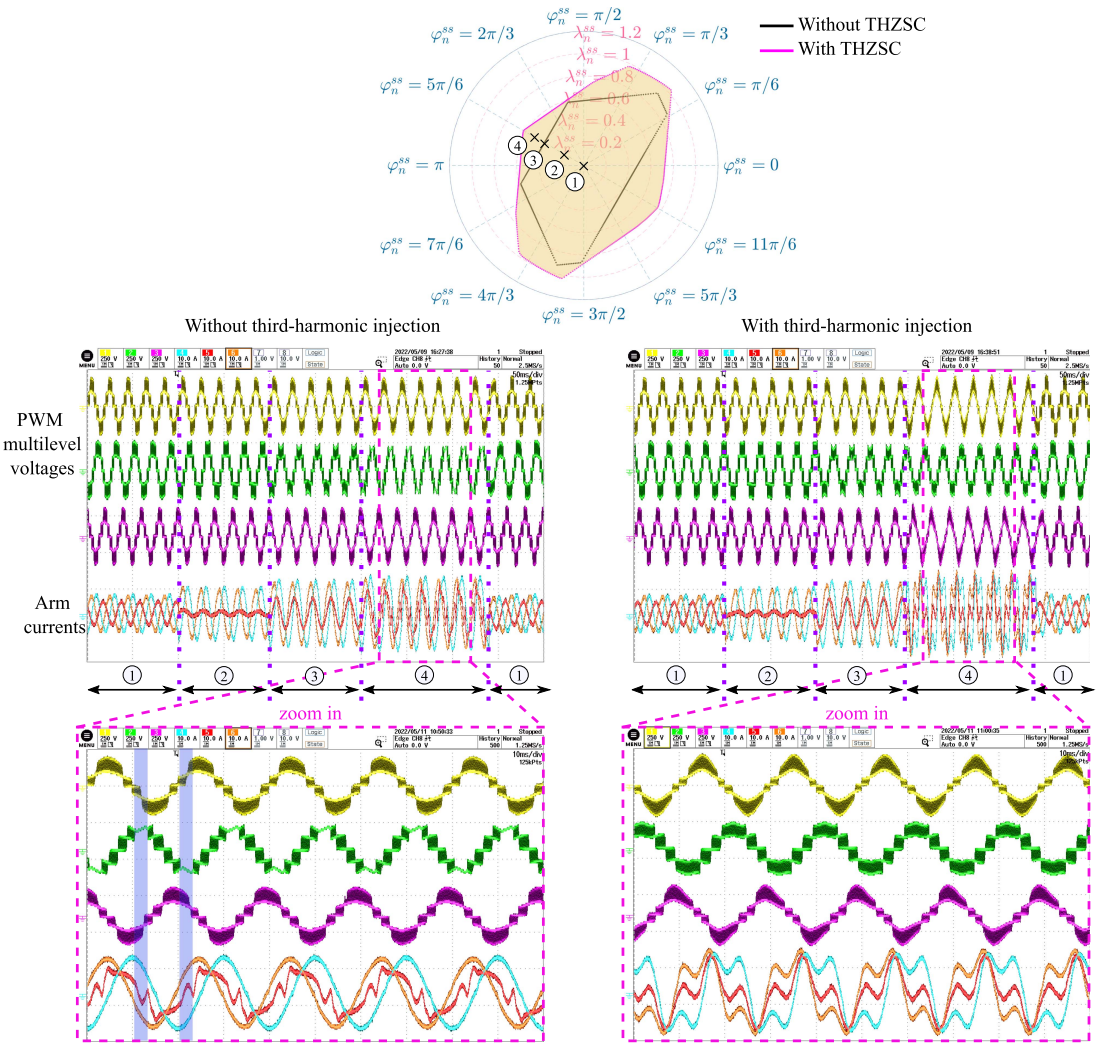

Fig. 9. Experimental waveforms for different negative-sequence current injections corresponding to ①, ②, ③, ④, for unbalanced grid voltages, and $\lambda_{pq}^{ss} = -0.5$. Left column: Without optimal THZSC injection. Right column: With optimal THZSC injection. Channels CH1, 2, and 3 show the PWM converter voltages v_x, and Channels CH4, 5, and 6 show the arm currents $i_{\text{arm}-x}$.

V. Experimental Results

This section contains experimental measurements that demonstrate the LC-StatCom's capacity to provide negative-sequence current while complying with the design limitations (i.e., no overmodulation). The experimental LC-StatCom prototype is connected to a 60-V rms line-to-neutral grid, generated by a GE&EL 15-kVA CINERGIA grid emulator. The inductors are sized to provide a rated voltage drop of about 4%. Each phase-arm of the prototype has two submodules built from IMPERIX PEH2015 full-bridge modules. The capacitors are chosen to offer a rated voltage oscillation of around 60%. The prototype system parameters are listed in Table II, and the experimental setup is shown in Fig. 7. The control system described in Section IV is implemented on an IMPERIX B-Box RCP 3.0 board, and executed at 20 kHz.

There are four experiments carried out. The LC-StatCom provides 50% of the positive-sequence rated current in all experiments ($\lambda_{pq}^{ss} = -0.5$), but the negative-sequence current values are different. The first two experiments investigate a balanced grid voltage condition, and the results are shown in Fig. 8. The other two experiments analyze an unbalanced grid voltage situation, and the results are shown in Fig. 9, in which the line-to-neutral grid voltage in phase a is 50% below its nominal value. In each set of experiments, some results consider the injection of the optimal THZSC, while the others do not. This displays the varied capabilities of injecting negative-sequence current when the LC-StatCom is producing 50% of the positive-sequence rated current. The delimiting negative-sequence polygonal compensation zones, as well as the four operational points evaluated for each experiment, are displayed at the top of Figs. 8 and 9. Note that the operating points corresponding to each of the negative-sequence current injections are indicated by crosses ①, ②, ③, and ④. The figures show the transient waveforms corresponding to the StatCom PWM multilevel voltages and arm currents during step changes among the different operating points. In addition, an expanded version of the steady state at operating point ④ is provided, where it is highlighted how

the proposed THZSC allows to enlarge the negative-sequence current range.

In Fig. 8, the different negative-sequence currents correspond to ①$(0,\ 5\pi/6)$, ②$(0.25,\ 5\pi/6)$, ③$(0.50,\ 5\pi/6)$, and ④ $(0.60,\ 5\pi/6)$. It is worth to mention that the operating point ④ is outside the polygonal orange region bounded by black lines, but inside the polygonal orange region bounded by magenta lines. Therefore, ④ produces overmodulation when THZSC is not considered, and this is highlighted, for the first period, using a blue color shading in the bottom-left plot of Fig. 8. It can be observed that during these intervals, the output voltage v_{bc} does not switch, and the arm current $i_{\text{arm}-bc}$ presents low-frequency distortion. However, when the proposed THZSC is injected, v_{bc} does switch, as shown in the bottom-right plot of Fig. 8, and, consequently, the LC-StatCom can provide the required current. This set of results is in close agreement with the respective simulation results shown in Fig. 3.

In Fig. 9, ①$(0,\ 5\pi/6)$, ②$(0.2,\ 5\pi/6)$, ③$(0.4,\ 5\pi/6)$, and ④ $(0.5,\ 5\pi/6)$. Phase-arm bc behaves similarly to the grid voltage balanced case in Fig. 8, in that, it exhibits capacitive behavior in ①, begins to process nearly zero power in ②, then changes to inductive mode in ③, and finally overmodulates in ④ when no THZSC is injected. Again, the proposed THZSC allows to enlarge the region of operation, and the results are in close agreement with the simulations depicted in Fig. 4.

VI. Conclusion

Potential capability of negative-sequence current injection in LC-StatComs with delta configuration, considering unbalanced grid conditions and THZSC injection, has been identified. These physical limits have been calculated using an LP model that takes into account the LC-StatCom dynamic behavior in the steady state, which, in turn, considers the intrinsic twice-fundamental-frequency capacitor voltage oscillation. The analysis reveals that the operational region expanded by injecting the optimal THZSC is defined by straight lines in a polar plane, resulting in a polygonal region. Furthermore, these straight lines depend on the capacitor size and the positive- and negative-sequence components of the grid voltages. As an example, the increase of the negative-sequence current compensating area is enlarged from 0.25π to 0.34π, i.e., 36% increase, when the capacitor size in the LC-StatCom is $C = 1.43$ mF. The presented analysis is validated by simulations in a high-power system, and experimentally in a down-scaled laboratory prototype, showing agreement with the derived operating bounds.

Appendix A
Fundamental-Frequency Zero-Sequence Current Calculation

Herein, the details of required FFZSC $\{\hat{I}^{ss}_{z1},\ \varphi^{ss}_{z1}\}$ and positive-sequence current angle φ^{ss}_{p} for mantaining the capacitor voltages bounded in the steady state are provided.

With the definition of the Cartesian-axis variables, (8) can be rewritten as follows:

$$
\begin{aligned}
e_{ab}(t) &= E_{abX}\cos(\omega t) + E_{abY}\sin(\omega t)\\
e_{bc}(t) &= E_{bcX}\cos(\omega t) + E_{bcY}\sin(\omega t)\\
e_{ca}(t) &= E_{caX}\cos(\omega t) + E_{caY}\sin(\omega t)\\
i^{ss}_{\text{arm}-ab}(t) &= I^{ss}_{abX}\cos(\omega t) + I^{ss}_{abY}\sin(\omega t)\\
i^{ss}_{\text{arm}-bc}(t) &= I^{ss}_{bcX}\cos(\omega t) + I^{ss}_{bcY}\sin(\omega t)\\
i^{ss}_{\text{arm}-ca}(t) &= I^{ss}_{caX}\cos(\omega t) + I^{ss}_{caY}\sin(\omega t)
\end{aligned}
\tag{34}
$$

where the voltage Cartesian $XY-$components correspond to

$$
\begin{aligned}
E_{abX} &= E_{nd} + E_{pd}\\
E_{abY} &= E_{nq}\\
E_{bcX} &= -\frac{1}{2}E_{nd} - \frac{1}{2}E_{pd} + \frac{\sqrt{3}}{2}E_{nq}\\
E_{bcY} &= -\frac{1}{2}E_{nq} - \frac{\sqrt{3}}{2}E_{nd} + \frac{\sqrt{3}}{2}E_{pd}\\
E_{caX} &= -\frac{1}{2}E_{nd} - \frac{1}{2}E_{pd} - \frac{\sqrt{3}}{2}E_{nq}\\
E_{caY} &= -\frac{1}{2}E_{nq} + \frac{\sqrt{3}}{2}E_{nd} - \frac{\sqrt{3}}{2}E_{pd}
\end{aligned}
\tag{35}
$$

which uses the projections of the phasors in (8) as intermediate variables to simplify the notation and further analysis, i.e., $E_{pd} = \hat{E}_p$, $E_{nd} = \hat{E}_n\cos(\theta_n)$, $E_{nq} = \hat{E}_n\sin(\theta_n)$. Similarly, for current Cartesian $XY-$components

$$
\begin{aligned}
I^{ss}_{abX} &= I^{ss}_{z1d} + I^{ss}_{nd} + I^{ss}_{pd}\\
I^{ss}_{abY} &= -I^{ss}_{z1q} + I^{ss}_{nq} - I^{ss}_{pq}\\
I^{ss}_{bcX} &= I^{ss}_{z1d} - \frac{1}{2}I^{ss}_{nd} - \frac{1}{2}I^{ss}_{pd} + \frac{\sqrt{3}}{2}I^{ss}_{nq} + \frac{\sqrt{3}}{2}I^{ss}_{pq}\\
I^{ss}_{bcY} &= -I^{ss}_{z1q} - \frac{1}{2}I^{ss}_{nq} + \frac{1}{2}I^{ss}_{pq} - \frac{\sqrt{3}}{2}I^{ss}_{nd} + \frac{\sqrt{3}}{2}I^{ss}_{pd}\\
I^{ss}_{caX} &= I^{ss}_{z1d} - \frac{1}{2}I^{ss}_{nd} - \frac{1}{2}I^{ss}_{pd} - \frac{\sqrt{3}}{2}I^{ss}_{nq} - \frac{\sqrt{3}}{2}I^{ss}_{pq}\\
I^{ss}_{caY} &= -I^{ss}_{z1q} - \frac{1}{2}I^{ss}_{nq} + \frac{1}{2}I^{ss}_{pq} + \frac{\sqrt{3}}{2}I^{ss}_{nd} - \frac{\sqrt{3}}{2}I^{ss}_{pd}
\end{aligned}
\tag{36}
$$

where $I^{ss}_{pd} = \hat{I}^{ss}_{p}\cos(\varphi^{ss}_{p})$, $I^{ss}_{pq} = \hat{I}^{ss}_{p}\sin(\varphi^{ss}_{p})$, $I^{ss}_{nd} = \hat{I}^{ss}_{n}\cos(\varphi^{ss}_{n})$, $I^{ss}_{nq} = \hat{I}^{ss}_{n}\sin(\varphi^{ss}_{n})$, $I^{ss}_{z1d} = \hat{I}^{ss}_{z1}\cos(\varphi^{ss}_{z1})$, $I^{ss}_{z1q} = \hat{I}^{ss}_{z1}\sin(\varphi^{ss}_{z1})$.

Note that the steady-state average powers, $P^{ss}_{x-\text{avg}}$ in (7), can be readily calculated using the coordinates of the output voltages, v^{ss}_{x}, and the arm currents, $i^{ss}_{\text{arm}-x}$, i.e., assuming a negligible voltage drop across R_{arm} in (5)

$$
P^{ss}_{x-\text{avg}} = \tfrac{1}{2}\begin{bmatrix} I^{ss}_{xX} & I^{ss}_{xY}\end{bmatrix}\begin{bmatrix} E_{xX} + \omega L_{arm} I^{ss}_{xY}\\ E_{xY} - \omega L_{arm} I^{ss}_{xX}\end{bmatrix}
\tag{37}
$$

which must satisfy $P^{ss}_{x-\text{avg}} = 0$, i.e., the vectors are orthogonal. Therefore, from condition $P^{ss}_{x-\text{avg}} = 0$, the next relationship among Cartesian $XY-$components can be obtained

$$
I^{ss}_{xX} = -I^{ss}_{xY}E_{xY}/E_{xX}.
\tag{38}
$$

And substituting the coordinate expressions (35) and (36) in (37), yields the following relationship:

$$\boldsymbol{F}\begin{bmatrix} I_{z1d}^{ss} \\ I_{z1q}^{ss} \\ I_{pd}^{ss} \end{bmatrix} + \boldsymbol{g} = \boldsymbol{T}_{\alpha\beta 0}\begin{bmatrix} P_{ab-\text{avg}}^{ss} \\ P_{bc-\text{avg}}^{ss} \\ P_{ca-\text{avg}}^{ss} \end{bmatrix} \tag{39}$$

where

$$\boldsymbol{F} = \begin{bmatrix} \frac{\sqrt{6}(E_{nd}+E_{pd})}{4} & -\frac{\sqrt{6}E_{nq}}{4} & \frac{\sqrt{6}E_{nd}}{4} \\ \frac{\sqrt{6}E_{nq}}{4} & \frac{\sqrt{6}(E_{nd}-E_{pd})}{4} & -\frac{\sqrt{6}E_{nq}}{4} \\ 0 & 0 & \frac{\sqrt{3}E_{pd}}{2} \end{bmatrix} \tag{40}$$

$$\boldsymbol{g} = \begin{bmatrix} \frac{\sqrt{6}\left(E_{pd}I_{nd}^{ss}-E_{nq}I_{pq}^{ss}\right)}{4} \\ -\frac{\sqrt{6}\left(E_{nd}I_{pq}^{ss}+E_{pd}I_{nq}^{ss}\right)}{4} \\ \frac{\sqrt{3}\left(E_{nd}I_{nd}^{ss}+E_{nq}I_{nq}^{ss}\right)}{2} \end{bmatrix} \tag{41}$$

with $\boldsymbol{T}_{\alpha\beta 0}$ as the power-conservative Clarke transformation matrix. Note that the system (39) has a single unique solution unless $\hat{E}_n = \hat{E}_p$, which represents the singularity point reported in [12], and corresponds to the condition where the linear equation system (39) is undetermined.

Also, it can be remarked that under balanced grid voltage conditions, i.e., $\hat{E}_n = 0$, the solution to (39) corresponds to $I_{z1d}^{ss} = -I_{nd}^{ss}$, $I_{z1q}^{ss} = -I_{nq}^{ss}$, $I_{pd}^{ss} = 0$, as reported in [11].

Note that the steady-state relationship (39) between the average ac-side powers $P_{x-\text{avg}}$ and the currents in the $dq0$ frame, can be extended for a transient in variables $\{I_{z1d},\ I_{z1q},\ I_{pd}\}$ and average powers $P_{x-\text{avg}}$ when the frequential transient behavior is much slower than the fundamental frequency ω, or when it has a quasi steady-state dynamical behavior [28]

$$\boldsymbol{F}\begin{bmatrix} I_{z1d} \\ I_{z1q} \\ I_{pd} \end{bmatrix} + \boldsymbol{g} = \boldsymbol{T}_{\alpha\beta 0}\begin{bmatrix} P_{ab-\text{avg}} \\ P_{bc-\text{avg}} \\ P_{ca-\text{avg}} \end{bmatrix}. \tag{42}$$

Appendix B
Look-up Table Generation

Herein, the procedural steps to follow for obtaining the optimal references that could be stored in a look-up table, which are provided by the "Linear Programming References Generation" block in Fig. 6 are explained.

1) Initialize variables $\{E_{pd},\ E_{nd},\ E_{nq},\ I_{pq}^{ss},\ \varphi_n^{ss}\}$ and parameters $\{C,\ n,\ V_{UB},\ \omega\}$.
2) Use $\{E_{pd},\ E_{nd},\ E_{nq}\}$ to calculate constants $\alpha_x,\ \beta_x,\ \gamma_x$ according to (13), and the Cartesian $XY-$components $\{E_{xX},\ E_{xY}\}$ according to (35).
3) Use $\{I_{pq}^{ss},\ \varphi_n^{ss},\ C,\ n,\ V_{UB},\ \omega\}$ and calculated values from *Step 2* to calculate lower bounds $lb_x(t)$, upper bounds $ub_x(t)$, and coefficients $a_x(t,\ \varphi_n^{ss})$, $q_{xX}(t)$, $q_{xY}(t)$, according to (15), (16), (17), (32), and (33), respectively.
4) Calculate column vectors $\boldsymbol{lb}_x$, $\boldsymbol{ub}_x$, $\boldsymbol{a}_x(\varphi_n^{ss})$, $\boldsymbol{q}_{xX}$, $\boldsymbol{q}_{xY}$ using the values of $lb_x(t)$, $ub_x(t)$, $a_x(t,\ \varphi_n^{ss})$, $q_{xX}(t)$, $q_{xY}(t)$ at $\omega t = \pi\eta/N_s$, according to (26), $\eta \in \{0,\ 1,\ \ldots,\ N_s - 1\}$ being the sample index and N_s the number of samples considered for discretization.
5) Calculate the LP matrices $\boldsymbol{A}(\varphi_n^{ss}) \in \mathbb{R}^{(6N_s+4)\times 6}$, $\boldsymbol{b} \in \mathbb{R}^{(6N_s+4)}$, $\boldsymbol{c} \in \mathbb{R}^6$ according to (31), (25), (30), respectively.
6) Solve the LP problem (23) in MATLAB (`X = linprog(f,A,b)`), with output `X` equal to the optimum of the optimization variables $\{\hat{I}_n^{ss},\ K_{ab}^{ss},\ K_{bc}^{ss},\ K_{ca}^{ss}, I_{z3X}^{ss},\ I_{z3Y}^{ss}\}$, and store the obtained `X` in a look-up table.
7) Repeat *Step 3–Step 6* for φ_n^{ss} in the range $[0,\ 2\pi)$.
8) Repeat *Step 3–Step 7* for normalized I_{pq}^{ss} in the range $[-1,\ 1]$.
9) Repeat *Step 2–Step 8* for grid voltage conditions of interest.

References

[1] G. Farivar, B. Hredzak, and V. G. Agelidis, "Reduced-capacitance thin-film H-bridge multilevel STATCOM control utilizing an analytic filtering scheme," *IEEE Trans. Ind. Electron.*, vol. 62, no. 10, pp. 6457–6468, Oct. 2015.

[2] G. Farivar, C. D. Townsend, B. Hredzak, J. Pou, and V. G. Agelidis, "Low-capacitance cascaded H-bridge multilevel StatCom," *IEEE Trans. Power Electron.*, vol. 32, no. 3, pp. 1744–1754, Mar. 2017.

[3] G. G. Farivar et al., "Cascaded H-bridge low capacitance static compensator with modular switched capacitors," *IEEE Trans. Ind. Electron.*, vol. 68, no. 7, pp. 5944–5954, Jul. 2021.

[4] X. Ge and F. Gao, "Flexible third harmonic voltage control of low capacitance cascaded H-bridge STATCOM," *IEEE Trans. Power Electron.*, vol. 33, no. 3, pp. 1884–1889, Mar. 2018.

[5] T. Isobe, L. Zhang, H. Tadano, J. A. Suul, and M. Molinas, "Control of DC-capacitor peak voltage in reduced capacitance single-phase STATCOM," in *Proc. IEEE 17th Workshop Control Model. Power Electron.*, 2016, pp. 1–8.

[6] E. R. Rodriguez, R. Leyva, G. G. Farivar, C. D. Townsend, and J. Pou, "Operation of the low-capacitance cascaded H-bridge StatCom under grid voltage swells," *IEEE Trans. Power Electron.*, vol. 37, no. 10, pp. 12552–12562, Oct. 2022.

[7] F. Z. Peng and J. Wang, "A universal STATCOM with delta-connected cascade multilevel inverter," in *Proc. IEEE 35th Annu. Power Electron. Specialists Conf.*, 2004, vol. 5, pp. 3529–3533.

[8] R. E. Betz, T. Summers, and T. Furney, "Symmetry compensation using a H-bridge multilevel STATCOM with zero sequence injection," in *Proc. IEEE Conf. Rec. Ind. Appl. Conf. 41st IAS Annu. Meeting*, vol. 4, 2006, pp. 1724–1731.

[9] Q. Song and W. Liu, "Control of a cascade STATCOM with star configuration under unbalanced conditions," *IEEE Trans. Power Electron.*, vol. 24, no. 1, pp. 45–58, Jan. 2009.

[10] M. Hagiwara, R. Maeda, and H. Akagi, "Negative-sequence reactive-power control by a PWM STATCOM based on a modular multilevel cascade converter (MMCC-SDBC)," *IEEE Trans. Ind. Appl.*, vol. 48, no. 2, pp. 720–729, Mar. 2012.

[11] H. Zhang, L. Angquist, S. Norrga, H.-P. Nee, and S. Ostlund, "Benchmark of high-power STATCOM topologies for flicker compensation," in *Proc. IEEE 18th Eur. Conf. Power Electron. Appl.*, 2016, pp. 1–10.

[12] E. Behrouzian and M. Bongiorno, "Investigation of negative-sequence injection capability of cascaded H-bridge converters in star and delta configuration," *IEEE Trans. Power Electron.*, vol. 32, no. 2, pp. 1675–1683, Feb. 2017.

[13] D. Lu, J. Zhu, J. Wang, J. Yao, S. Wang, and H. Hu, "A simple zero-sequence-voltage-based cluster voltage balancing control and the negative sequence current compensation region identification for star-connected cascaded H-bridge STATCOM," *IEEE Trans. Power Electron.*, vol. 33, no. 10, pp. 8376–8387, Oct. 2018.

[14] E. Rodriguez Ramos, R. Leyva, G. G. Farivar, C. D. Townsend, and J. Pou, "Operating limits for low-capacitance cascaded H-bridge static compensators," *IEEE Trans. Power Electron.*, vol. 37, no. 3, pp. 3421–3433, Mar. 2022.

[15] Y. Yu, G. Konstantinou, B. Hredzak, and V. G. Agelidis, "Power balance of cascaded H-bridge multilevel converters for large-scale photovoltaic integration," *IEEE Trans. Power Electron.*, vol. 31, no. 1, pp. 292–303, Jan. 2016.

[16] O. J. K. Oghorada and L. Zhang, "Unbalanced and reactive load compensation using MMCC-based SATCOMs with third-harmonic injection," *IEEE Trans. Ind. Electron.*, vol. 66, no. 4, pp. 2891–2902, Apr. 2019.

[17] Y. Yu, G. Konstantinou, B. Hredzak, and V. G. Agelidis, "Power balance optimization of cascaded H-bridge multilevel converters for large-scale photovoltaic integration," *IEEE Trans. Power Electron.*, vol. 31, no. 2, pp. 1108–1120, Feb. 2016.

[18] D. Lu, C. Sha, Y. Yu, X. Li, H. Hu, and Y. Xing, "Flexible nonsinusoidal zero sequence voltage injection method to extend negative sequence current compensation range for star-connected CHB STATCOM," *IEEE Trans. Power Electron.*, vol. 36, no. 10, pp. 11357–11371, Oct. 2021.
[19] D. d. Carmo Mendonça, J. M. Soares Callegari, A. F. Cupertino, H. A. Pereira, S. I. Seleme Junior, and R. Teodorescu, "Delta-CHB STATCOM with reduced energy storage requirements based on third harmonic injection," in *Proc. IEEE Braz. Power Electron. Conf.*, 2021, pp. 1–7.
[20] E. R. Rodriguez et al., "Enhancing inductive operation of low-capacitance cascaded H-bridge StatComs using optimal third-harmonic circulating current," *IEEE Trans. Power Electron.*, vol. 36, no. 9, pp. 10788–10800, Sep. 2021.
[21] K. E. Lucas et al., "Robust control of interconnected power electronic converters to enhance performance in DC distribution systems: A case of study," *IEEE Trans. Power Electron.*, vol. 36, no. 4, pp. 4851–4863, Apr. 2021.
[22] E. Chatzinikolaou and D. J. Rogers, "Performance evaluation of duty cycle balancing in power electronics enhanced battery packs compared to conventional energy redistribution balancing," *IEEE Trans. Power Electron.*, vol. 33, no. 11, pp. 9142–9153, Nov. 2018.
[23] A. C. Luna, N. L. Diaz, M. Graells, J. C. Vasquez, and J. M. Guerrero, "Mixed-integer-linear-programming-based energy management system for hybrid PV-wind-battery microgrids: Modeling, design, and experimental verification," *IEEE Trans. Power Electron.*, vol. 32, no. 4, pp. 2769–2783, Apr. 2017.
[24] H. Zhixing et al., "Circulating current derivation and comprehensive compensation of cascaded STATCOM under asymmetrical voltage conditions," *IET Gener., Transmiss. Distrib.*, vol. 10, no. 12, pp. 2924–2932, 2016.
[25] M. A. Goberna and M. Lopez-Cerda, *Linear Semi-Infinite Optimization*. Hoboken, NJ, USA: Wiley, 1998.
[26] C. D. Townsend et al., "Identifying circulating currents and zero-sequence voltages for reduction in stored capacitor energy in modular multilevel converters," *IEEE Trans. Ind. Electron.*, vol. 68, no. 1, pp. 454–465, Jan. 2021.
[27] A. I. Bratcu and R. Teodorescu, "State-feedback control of grid and circulating current in modular multilevel converters," *IFAC-PapersOnLine*, vol. 53, no. 2, pp. 12396–12401, Jul. 2020.
[28] F. Verhulst, *Methods and Applications of Singular Perturbations: Boundary Layers and Multiple Timescale Dynamics*. New York, NY, USA: Springer, 2005.

Ezequiel Rodriguez Ramos (Member, IEEE) was born in Tarragona, Spain, in 1994. He received the bachelor's degree in electrical engineering and the master's degree in engineering and technology of electronic systems (topping the 2012 and 2016 graduating cohorts as valedictorian) from Universitat Rovira i Virgili, Catalonia, Spain, in 2016 and 2017, respectively, and the Ph.D. degree in electrical engineering from Nanyang Technological University (NTU), Singapore, in 2022.

He is currently working as a Postdoctoral Research Fellow with the Energy Research Institute, NTU (ERI@N), Singapore. His research interests include modeling and the control of power electronic converters, with an emphasis on modular multilevel cascade converters for energy storage and FACTS applications.

Dr. Ezequiel was the recipient of the 2022 Best Thesis Award from NTU.

Ramon Leyva (Senior Member, IEEE) received the M.Sc. and Ph.D. degrees in telecommunication engineering from the Technical University of Catalonia (UPC)-Barcelona Tech, Barcelona, Spain, in 1992 and 2000, respectively.

He was a Visiting Professor with LAAS-CNRS, Toulouse, France, from 2002 to 2003, and in 2009 and 2010, and with the COPEC-University of Colorado at Boulder, USA, in 2012. He is currently an Associate Professor with the Department of Electronic, Electrical and Automatic Engineering, Universitat Rovira i Virgili, Tarragona, Spain. He has coauthored more than 100 scientific publications, two books and one patent, and has been involved more than 20 R&D projects. His research interests include nonlinear and robust control of power converters and renewable energy.

Dr. Leyva serves as Reviewer for several IEEE and IET scientific publications.

Glen G. Farivar (Senior Member, IEEE) received the B.Sc. degree in electrical engineering from the Nooshirvani Institute of Technology, Babol, Iran, in 2008, the M.Sc degree in power electronics from the University of Tehran, Tehran, Iran, in 2011, and the Ph.D. degree in electrical engineering from the University of NSW Australia, Syndey, Australia, in 2016.

He is currently with Nanayang Technologilal University, Singapore, as a Senior Research Fellow with the Energy Research Institute (ERI@N), and a co-Director of Power Electronics and Applications Research Lab. He is a co-Founder of SciLeap which aims to promote research integrity, accessibility and openness. His research interests include renewable energy systems, high power convertors, energy storage, FACTS, and electric vehicles.

Christopher D. Townsend (Member, IEEE) received the B.E. and Ph.D. degrees in electrical engineering from the University of Newcastle, Callaghan NSW, Australia, in 2009 and 2013, respectively.

He spent three years working with ABB Corporate Research, Zürich, Sweden working on next-generation high-power converter technologies. Since then he has held various post-doctoral research positions including at the University of New South Wales, Sydney, NSW, Australia, the University of Newcastle, and Nanyang Technological University, Singapore. In 2019, he joined the Department of Electrical, Electronic and Computer Engineering, University of Western Australia, Crawley, WA, Australia, as a Senior Lecturer. He has authored more than 60 published technical papers and has been involved in several industrial projects and educational programs in the field of power electronics. His research interests include topologies and modulation strategies for multilevel converters applied in power systems, renewable energy integration and electric vehicle applications.

Dr. Townsend is a member of the IEEE Power Electronics and Industrial Electronics societies.

Josep Pou (Fellow, IEEE) received the B.S., M.S., and Ph.D. degrees in electrical engineering from the Technical University of Catalonia (UPC)-Barcelona Tech, Barcelona, Spain, in 1989, 1996, and 2002, respectively.

In 1990, he joined the faculty of UPC as an Assistant Professor, where he became an Associate Professor, in 1993. From February 2013 to August 2016, he was a Professor with the University of New South Wales (UNSW), Sydney, NSW, Australia. He is currently a Professor with the Nanyang Technological University (NTU), Singapore, where he is Cluster Director of Power Electronics at the Energy Research Institute, NTU (ERI@N) and co-Director of the Rolls-Royce at NTU Corporate Lab. From February 2001 to January 2002, and February 2005 to January 2006, he was a Researcher with the Center for Power Electronics Systems, Virginia Tech, Blacksburg, VA, USA. From January 2012 to January 2013, he was a Visiting Professor with the Australian Energy Research Institute, UNSW. He has authored more than 400 published technical papers and has been involved in several industrial projects and educational programs in the fields of power electronics and systems. His research interests include modulation and control of power converters, multilevel converters, renewable energy, energy storage, power quality, HVdc transmission systems, and more-electrical aircraft and vessels.

Dr. Pou was the recipient of the 2018 IEEE Bimal Bose Award for Industrial Electronics Applications in Energy Systems. He is the Associate Editor for the IEEE JOURNAL OF EMERGING AND SELECTED TOPICS IN POWER ELECTRONICS. He was co-Editor-in-Chief and Associate Editor for the IEEE TRANSACTIONS ON INDUSTRIAL ELECTRONICS.